



Zhuo Yang

Associate at National Institute of Standards and Technology,
100 Bureau Dr,
Gaithersburg, MD 20899
e-mail: zhuo.yang@nist.gov

Jaehyuk Kim

Associate at National Institute of Standards and Technology,
100 Bureau Dr,
Gaithersburg, MD 20899
e-mail: jaehyuk.kim@nist.gov

Yan Lu¹

National Institute of Standards and Technology,
100 Bureau Dr,
Gaithersburg, MD 20899
e-mail: yan.lu@nist.gov

Albert Jones

National Institute of Standards and Technology,
100 Bureau Dr,
Gaithersburg, MD 20899
e-mail: albert.jones@nist.gov

Paul Witherell

National Institute of Standards and Technology,
100 Bureau Dr,
Gaithersburg, MD 20899
e-mail: paul.witherell@nist.gov

Ho Yeung

National Institute of Standards and Technology,
100 Bureau Dr,
Gaithersburg, MD 20899
e-mail: ho.yeung@nist.gov

Hyunwoong Ko

Arizona State University,
AZ 85212
e-mail: hyunwoong.ko@asu.edu

Enhancing Part Quality Management Using a Holistic Data Fusion Framework in Metal Powder Bed Fusion Additive Manufacturing

Metal powder bed fusion additive manufacturing (AM) processes have gained widespread adoption for the ability to produce complex geometries with high performance. However, a multitude of factors still affect the build process, which significantly impacts the adoption rate. This, in turn, leads to great challenges in achieving consistent and reliable part quality. To address this challenge, simulations and measurements have been progressively deployed to provide valuable insights into the quality of individual builds. This paper proposes an AM data fusion framework that combines data sources beyond a single-part, development cycle. Those sources include the aggregation of measurements from multiple builds and the outputs from their related models and simulations. Both can be used to support decision-makings that can improve part quality. The effectiveness of the holistic AM data fusion framework is illustrated through three use case scenarios: one that fuses process data from a single build, one that fuses data from a build and simulation, and one that fuses data from multiple builds. The case studies demonstrate that a data fusion framework can be applied to effectively detect over-melting scan strategies, monitor material melting conditions, and predict down-skin surface defects. Overall, the proposed method provides a practical solution for enhancing part quality management when individual data sources or models have intrinsic limitations. [DOI: 10.1115/1.4064528]

Keywords: additive manufacturing, process planning, data fusion, predictive modeling, information management, process modeling for engineering applications, qualification, verification, and validation of computational models

1 Introduction

Additive manufacturing (AM) technologies enable the fabrication of complex geometries of heterogeneous metal parts. Assuring the quality of those parts is one of the biggest challenges for manufacturers to adopt AM technologies [1]. The unique layer-by-layer AM building process expands the design options, freedoms, and

spaces over traditional, subtractive, manufacturing methods [2]. However, when using a laser powder bed fusion (L-PBF) process, these expansions increase the difficulty of the process and part quality control. These difficulties are due to the associated complex physics and subsequent repeated cycles of material melting and solidification [3,4]. To address these difficulties, AM developers have made substantial efforts to leverage simulation, physics-based, and in situ monitoring models. Developers are now using both for process parameter development, scan strategy optimization, process monitoring, and process control.

Physics-based and simulation models are frequently used in AM design and process planning to optimize AM builds for qualified parts. In L-PBF, this often means simulating, predicting, and

¹Corresponding author.

Manuscript received July 23, 2023; final manuscript received January 9, 2024; published online March 5, 2024. Assoc. Editor: Krishnanand Kaipa.

This work is in part a work of the U.S. Government. ASME disclaims all interest in the U.S. Government's contributions.

monitoring melt pool behaviors. Finite element analysis (FEA) and computational fluid dynamics (CFD) are prevalent in predicting melt pool behavior in L-PBF [5]. FEA focuses on predicting the temperature profile during the process [6] or simulating residual stress and part deformation [7]. CFD uses more complex computations to simulate the details of the melt pool formation [8].

In contrast to physics-based and simulation modeling approaches, data-driven modeling approaches aim to build statistical correlations between the given input variables and predicted outputs without fully understanding the underlying physics. Data-driven models have been successfully used in scenarios such as representing process–structure–property relationships for AM process scan strategy optimization [9] and correlating process parameters with melting thermal conditions and part quality [10–12].

In-process monitoring data can further improve the quality of AM parts. Since measurements based on a single sensing method can provide limited information about a printing process, multi-modal, in situ monitoring data types are usually required to fully evaluate process stability and accurately predict part defects [13]. Fusing multi-model data types became popular in the 1990s for automatic target recognition, target tracking, automated situation assessment, and smart weapons [14,15].

In AM, data fusion scenarios include multi-modal process monitoring and control, AM process structure property (PSP) relationship identification through advanced analytics, and AM qualification through multi-modal data sets. Each of these scenarios can employ co-processing and fusion at three individual data levels—raw data, feature, and decision levels—or a combination of the three, as defined in the Joint Directors of Laboratories (JDL) model [16]. Raw data fusion encompasses a simple concatenation of measurements in the same regions of space and time, facilitating the discovery of information. Feature-level fusion includes processing raw data into meaningful features and then conflating them, which allows for the estimation of the states of a system. Decision-level fusion combines decisions derived from individual data sources to support a final response.

Currently, however, raw-data-level fusion has several weaknesses, including high-dimensional data challenges and data unbalance issues. Decision-level data fusion is less explored due to the difficulty in adequately explaining a fusion result and conducting a control to influence it. Feature-level fusion has the greatest potential to support broader AM qualification challenges but requires provisional strategies for data dimension reduction, feature extraction, and conflation. For a more robust approach, Yang et al. [17] proposed a multi-scale hierarchical AM data fusion framework that combines multi-modal in-process AM data for process monitoring and control.

This paper extends the authors' 2021 study and proposes a new AM data fusion framework that aggregates data sources from different systems and builds models and simulations based on the result of that aggregation. Our new fusion approach will further improve AM part quality and facilitate decision-making. Section 2 describes the holistic data fusion framework (HDFFF). In Sec. 3, we detail the experimental design and present three data fusion scenarios based on the framework to illustrate the methodology and demonstrate effectiveness. These case studies involve multiple AM datasets, models, and algorithms. Section 4 summarizes the main findings and outlines future research directions. The last section briefly discusses the challenges and future work.

2 Problem Formulation

Multi-scale, hierarchical, AM data fusion is a technique to combine datasets from a single build [17]. In-process AM data fusion can be organized in a spatial reference frame. Data fusion in L-PBF generally happens at four spatial scales: pointwise, trackwise, layerwise, and partwise. Each scale goes from micro to macro. Pointwise fusion combines single-point sensor measurements, which are based on the associated process commands, for process anomaly detection or feedback loop control. Trackwise fusion integrates in

situ monitoring data from individual tracks to detect printing faults and apply iterative learning control. Layerwise fusion combines and processes multi-modality sensing data at the layer level. These data can reflect the cross-sectional quality of the AM part. Finally, partwise fusion is associated with the 3D part geometry and material structure, both of which can be used directly for part quality prediction and certification. Each of these scales can affect data analysis, feature extraction, and decision-making. For example, feature extraction and control optimization for melt pool formation require pointwise fusion. Nevertheless, partwise fusion focuses more on part quality characterization and optimization.

Our previous paper introduced the data fusion concept but for only one AM build and process [17]. The holistic AM data fusion goes beyond the use of data from a single build by combining data from simulations and other builds or systems to enable or improve inferences and decision-makings. Data generated from other processes and simulations can be thought of as raw data, feature, and decision-level data fusion, as shown in Fig. 1. The central routine of the HDFFF captures the original scale of fused datasets from a single AM build. The right routine of the framework denotes that modeling and simulation data can be combined at all three scales to support inferences and decision-makings for the current build. The left routine of the framework indicates that the data fusion concept can expand to multi-builds on the same AM system or even data generated from different AM systems. The blue arrow pointing to “Model” transforms features and data into the model instead of directly importing the main routine. This way may reduce the difficulty of direct fusion.

To leverage the “AM HDFFF,” data can be (1) fused directly to the current build-development process for decision-making or (2) used to create, validate, and enhance simulation models. Then, the simulation results can be fused to the current build part quality management. When executing a simple AM build process, HDFFF can be further elaborated with subprocesses. Examples include recoating, heating and cooling, and their designated sensors, as well as submodels that simulate various subprocess signatures against the measurement data. Generally, fusing simulation data with measurement data at the subprocess and process levels can improve the stability of both. Note that the subprocess approach provides better traceability for part-defect analysis.

The framework in Fig. 1 shows a simplified structure of the three routines. However, real AM applications usually have more complex data structures that increase the difficulty of implementing data fusion. AM data are naturally hierarchical and typically asynchronous according to their multi-physics behavior. Consequently, the HDFFF must include multiple builds and simulations that involve complex data-processing mechanisms at the raw data, feature, and decision levels. Based on the data structure in the scope of this framework, we differentiate data-processing mechanisms into two types: parallel and sequential. Both can be performed at varying dimensional scales and different sampling rates.

The parallel mechanism applies spatial and temporal fusion to datasets within one build in parallel [18,19], as shown in Fig. 2. “Parallel” indicates that the datasets can be collected at the same time during the process, but they do not necessarily have the same sampling rates. Datasets could be captured by different sensors or methods. For example, a Galvo encoder captures the laser position during the build. Meanwhile, the co-axial camera captures melt pool images. Fusing these two datasets can help identify localized melting conditions in the part. Multiple datasets can also be captured by a single sensor under different configurations. For example, multiple overview images can be captured by a tower camera—using different flashlights—placed in the build chamber at different locations. Fusing these images can provide details about the recoated powder bed or the just exposed build surface.

The sequential data fusion mechanism attempts to fuse data from multiple AM processes. Sequential AM data fusion can merge datasets to compensate for missing information. Figure 3 shows an example of fusing data from two separate AM processes. In this example, the datasets are generated from a similar physical

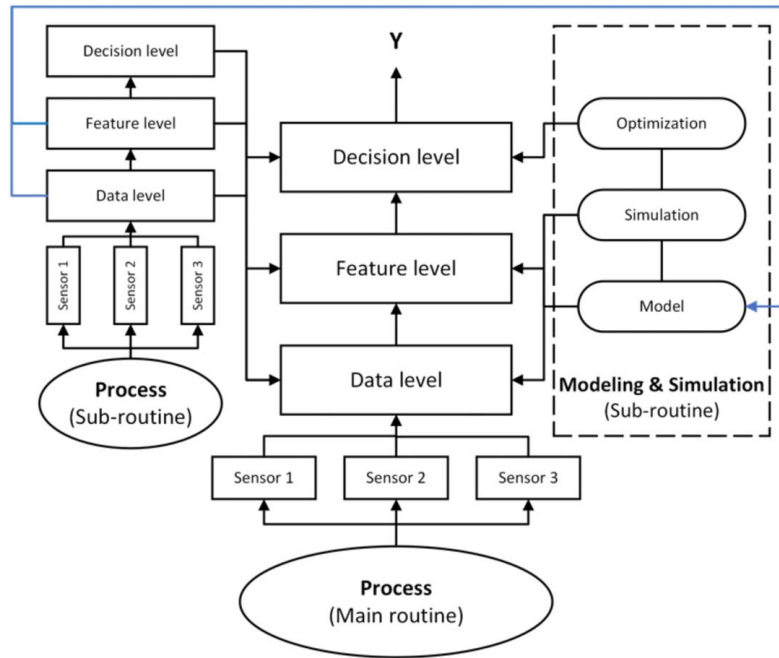


Fig. 1 AM HDFS with multiple systems and model

environment that could substitute the information that is missing from the main process. That missing information can be used as inputs to transfer learning with pre-trained models, such as deep learning ResNet, which may help to migrate knowledge between the multiple parts of the framework [20]. Figure 3 shows that subprocess 2 is not monitored in process 1. The data generated from subprocess 2 can be leveraged for process 1 monitoring and control.

The success of the proposed fusion mechanism depends on the actual features of the processes and subprocesses. Thus, extracting those features should be conducted before the fusion mechanism can be implemented. Additionally, extracted features from another build or system can be combined with the features extracted from the current build data directly. Another path to fuse the data from earlier processes into a new process is through modeling and simulation. In this case, the existing data are used to create a new model or validate and enhance an existing model. Simulations can run the models to generate data to be fused with the data from the process of concern. Usually, it is hard to justify direct data combinations from various builds because it requires a perfect match between the two processes. Instead, most cases employ certain transformations of data into knowledge first, such as models, before measurement and simulation data fusion. This way can reduce fusion complexity between different processes.

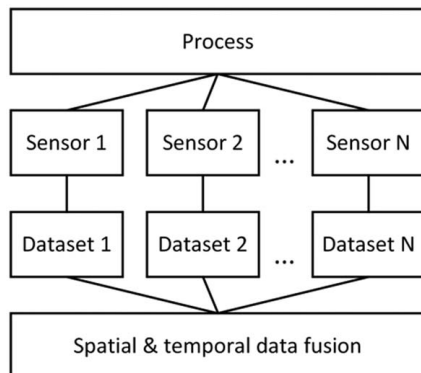


Fig. 2 Parallel data fusion mechanism

These two mechanisms provide fundamental approaches for applying HDFS. However, in most cases, the two mechanisms must be mixed. Furthermore, complex AM data fusion problems usually involve data co-processing at the subprocess level.

3 Case Studies

This section presents three case studies demonstrating the HDFS for L-PBF quality management under different scenarios. The first case study uses a parallel mechanism to fuse in situ melt pool images and laser position to identify over-melting regions. In situ data registration is heavily involved in formulating the fusion. The second case study has a similar parallel mechanism but fuses simulation results into data-driven modeling to improve melt pool prediction. The last case study incorporates parallel and sequential mechanisms to fuse multiple AM datasets from different systems and builds under a complex situation. The fused data are able to

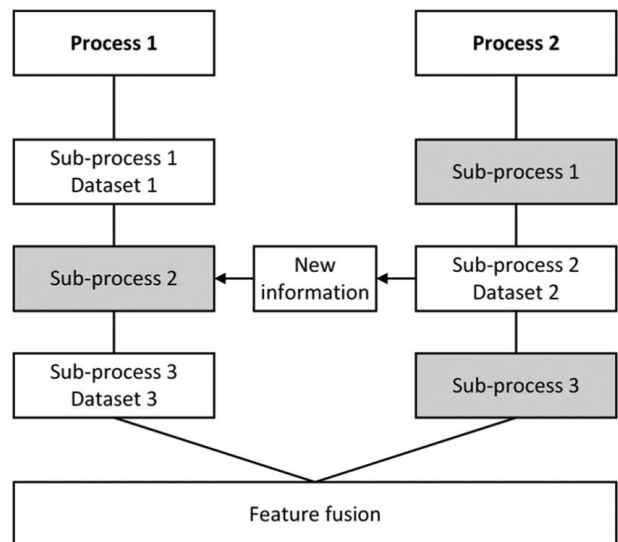


Fig. 3 Sequential data fusion mechanism

Table 1 Process parameters and sampling rates all experiments

	Setting
Laser power infilling (W)	195
Laser power pre-contour (W)	100
Laser spot size (μm)	80
Layer thickness (μm)	20
Co-axial camera sampling rate (image/s)	10,000

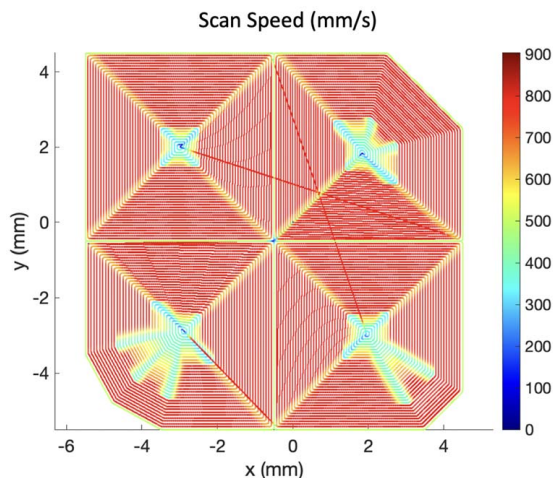
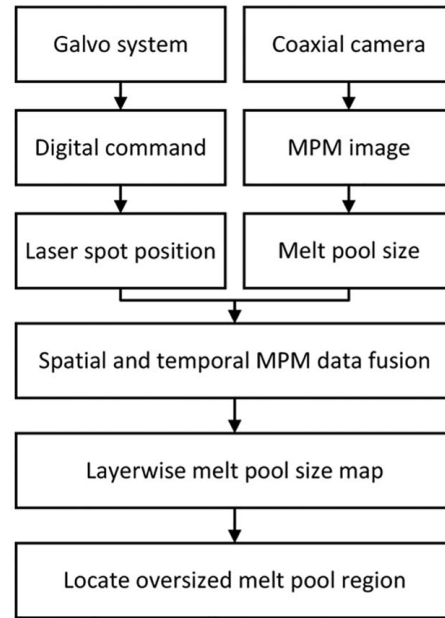
predict 3D remelting conditions based on 2D melt pool surface measurements. As-built part geometry estimation is the final output of this scenario, which belongs to partwise-level fusion.

3.1 Experimental Method. All case studies use the data collected from the Additive Manufacturing Metrology Testbed (AMMT) at the National Institute of Standards and Technology (NIST). AMMT is an open-platform metrology instrument that enables flexible control and measurement of the L-PBF process [21,22]. It is equipped with the capability to realize precise laser beam control. AMMT uses time-stepped digital commands to update laser position, power, diameter, and measurement device triggers at every $10\ \mu\text{s}$. Therefore, AMMT supports continuous laser power variation, and the monitoring signals can be fully synchronized back to the laser positions. Three experiments were conducted on AMMT to illustrate the following case studies. All experiments deploy the same process parameters and sampling rate. Scan strategies are different from each other.

Table 1 lists the process and sensor settings. Details specific to each case study will be introduced in each subsection. Laser poser infilling is used while scanning the cross-section within the part outline. Laser power pre-contour is the scan only on the part outline.

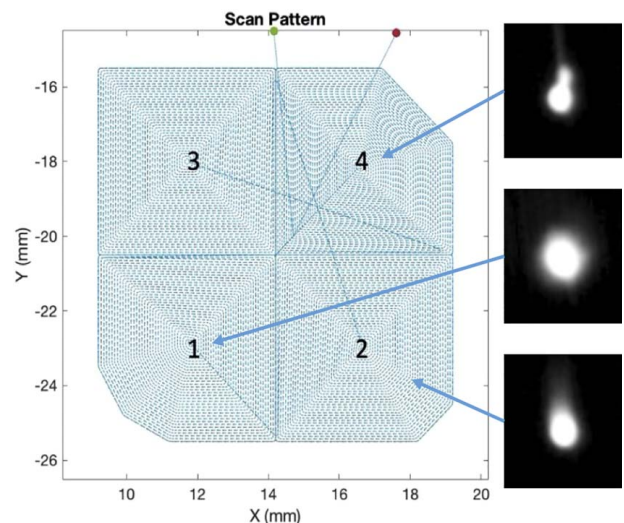
3.2 Identify Over-Melting Region. This case study fuses the melt pool monitoring (MPM) images and digital command data from a single-layer experiment conducted on AMMT [9]. The experiment uses a concentric spiral-in pattern with constant laser power for infilling and pre-contour. This single-layer build was divided into four islands. This pattern is mostly used for parts that have larger cross-sectional areas. Multiple islands can patch the entire layer with a shorter individual laser path. The nominal scan speed of infilling is set to 800 mm/s and reduced during turns. The nominal scan speed of pre-contour is 900 mm/s. Figure 4 plots the scan speed on the scan path. The color scale marks the scan speed from 0 to 900 mm/s.

Figure 5 details the data fusion mechanism for this case study. Galvo system uses time-stepped digital commands to control the

**Fig. 4 Programmed scan speed of the part****Fig. 5 Detailed parallel mechanism of the first case study**

laser position. Meanwhile, co-axial camera captures in situ MPM images during the build. The individual position and image data points are both at the pointwise level. Laser position extracted from digital commands and melt pool size measured from MPM satisfy parallel data fusion mechanism. The spatial and temporal data fusion can fully register the melt pool size at the layerwise level. Melt pool size distribution from fused maps is the key feature for identifying over-melting regions. In this case, the melt pool size is represented by the melt pool area. In the end, the oversized melt pool region is marked and recognized as over-melting due to abnormal melting conditions.

The experiment uses 214,297 digital commands to build the 10 mm \times 10 mm single-layer part. The scanning process took 2.14 s and collected 20,902 MPM images. Melt pool size is measured by counting pixels within the melt pool outline that are detected using the Canny Edge Detection method. The data fusion technique synchronized measured size to laser position based on the co-axial camera trigger in the digital command [17]. A fully registered melt pool scattering position would be used to construct the map by interpolating the unbalanced data. Figure 6

**Fig. 6 Synchronizing MPM images to their positions**

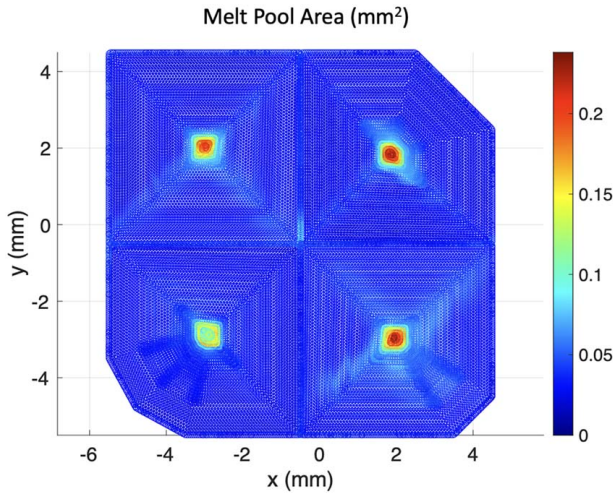


Fig. 7 Melt pool size distribution of the single-layer part

demonstrates the data fusion process from each individual MPM image to its position.

Figure 7 shows the melt pool size map from data fusion. In this figure, the color bar scales the size from small to large. The island centers that always scanned at the end have significantly oversized melt pools than other locations.

Oversized melt pools usually denote over-melting or excess melting flow [8]. Thus, it is possible to use this melt pool size map to identify over-melting regions. The edge detection technique outlines oversized regions. Finally, four over-melting regions were identified, which are marked by black ink, shown in Fig. 8.

A microscopic image was deployed to verify the result. Figure 9(a) is the raw microscopic image covering the entire layer. The texture on the surface is mostly identical to the scan pattern. Four over-melting holes at the island center are observed. Figure 9(b) overlays the predicted over-melting regions (red line) on top of the microscopic image. The alignment of two images is based on the part shape. As shown, the position and size of over-melting regions extracted from data fusion agree with microscopy.

This case study demonstrates a simple scenario of data fusion of two datasets from the same build. Fusion is based on a parallel mechanism. Before fusion, melt pool characteristics and position are only extractable information from the raw data. Data fusion connected these two datasets and generated a melt pool melting map, which is used to identify the over-melting regions. A microscopic image has verified the conclusions. It approves that HDFF can be

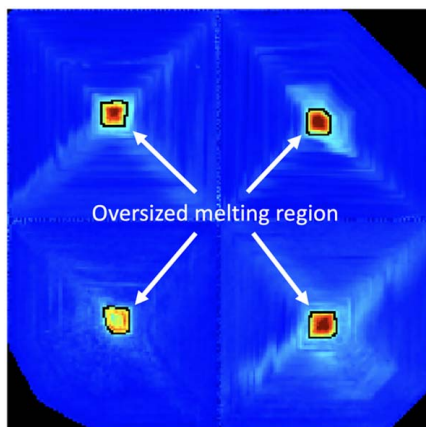


Fig. 8 Oversized melt pool region detected by edge detection

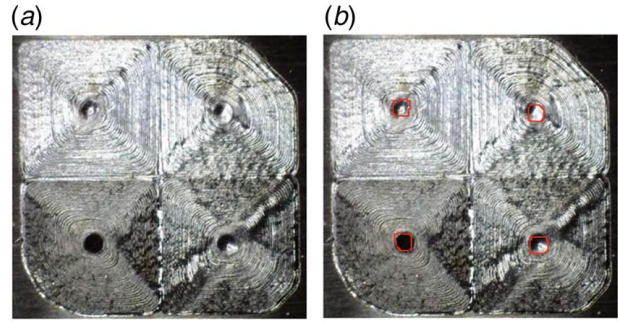


Fig. 9 Result verification using microscopic image: (a) is original microscopic image and (b) stacks the identified over-melting region to (a) for comparison

used to improve the process monitoring of a single build for better part quality control, for example, by adjusting process parameters on the fly.

3.3 Predict Melt Pool Size Based on Scan Strategy. Data fusion in this case study fuses FEA simulation and in situ melt pool measurement to improve melt pool size prediction. A 3D build experiment was conducted on AMMT to provide the in situ melt pool measurement. This experiment creates 12 nominally identical parts within the same build on a wrought nickel alloy 625 (IN625) substrate cut to 100 mm × 100 mm × 12.5 mm. All 12 parts have the same geometry but different scan strategies [23]. This case study selects three scan patterns: (1) regular skywriting, (2) island skywriting, and (3) island spiral concentrating [24]. All process parameters are the same as in the previous two case studies.

Similarly, the parallel mechanism applies to this scenario. Figure 10 shows the detailed mechanism of this case study. The same process parameters, such as scan path and laser power, are imported to the FEA model and sent to the AM machine. The simulated melt pool temperature and the measured melt pool size were combined by the “grey-box” modeling method [25]. On the measurement side, melt pool size is first registered based on the same procedure in Sec. 3.2.

The input variables for the FEA simulation are laser power 195 W, scan speed 800 mm/s, and the scan path. As shown in

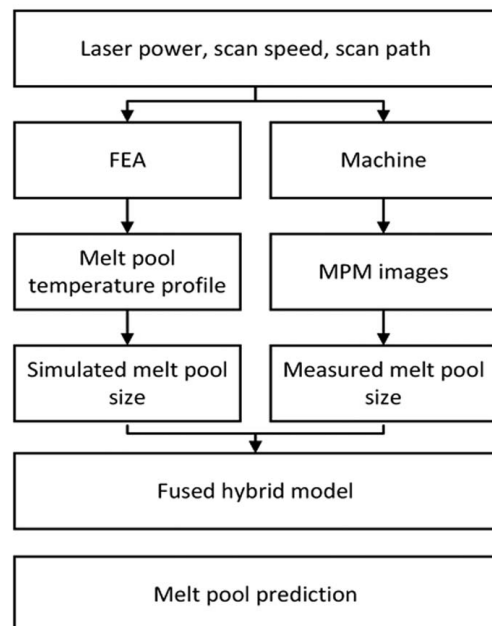


Fig. 10 Detailed parallel mechanism of the second case study

Fig. 11, FEA model can estimate the temperature of each layer in L-PBF. Scan path includes three patterns: regular skywriting from the bottom right corner to the top left corner, island skywriting, and island spiral concentrating [24]. An FEA model incorporating the laser input and scan speed can predict each layer's melt pool size distribution. The heatmap uses a color gradient to draw the oversized (red) and undersized (blue) regions.

The data fusion uses the grey-box modeling method to integrate the simulation model and the experimental data [6,26]. For patterns 1–3, 2661, 3884, and 6884 MPM images are collected, respectively. For each pattern, data are divided into 50%–50% for training and testing. The purpose of using less training data is to test the model performance with a small sample size. The hybrid models are presented in Fig. 12. Table 2 compares the normalized root mean square error (NRMSE) between the Simulation and Hybrid models.

This case study has an increased complexity of data fusion. Beyond MPM melt pool features extraction and fusion with laser position, it requires a fusion to create a hybrid model with an FEA simulation and measurement data. Experimental measurements are generally considered ground truth since they are always specific to a build. However, measurement data could include noises that compromise their usability. On the other hand, though an FEA model can simulate a build process that covers most of the physics, it has limitations in capturing all building conditions, such as machine specifics and environmental conditions. These limitations trigger the idea of data fusion of measurement and simulation results. Data fusion, which combines both, provides noticeable prediction improvement of the hybrid model. In addition, training a surrogate model from the FEA-based simulations can reduce the computational time and use fewer experimental samples.

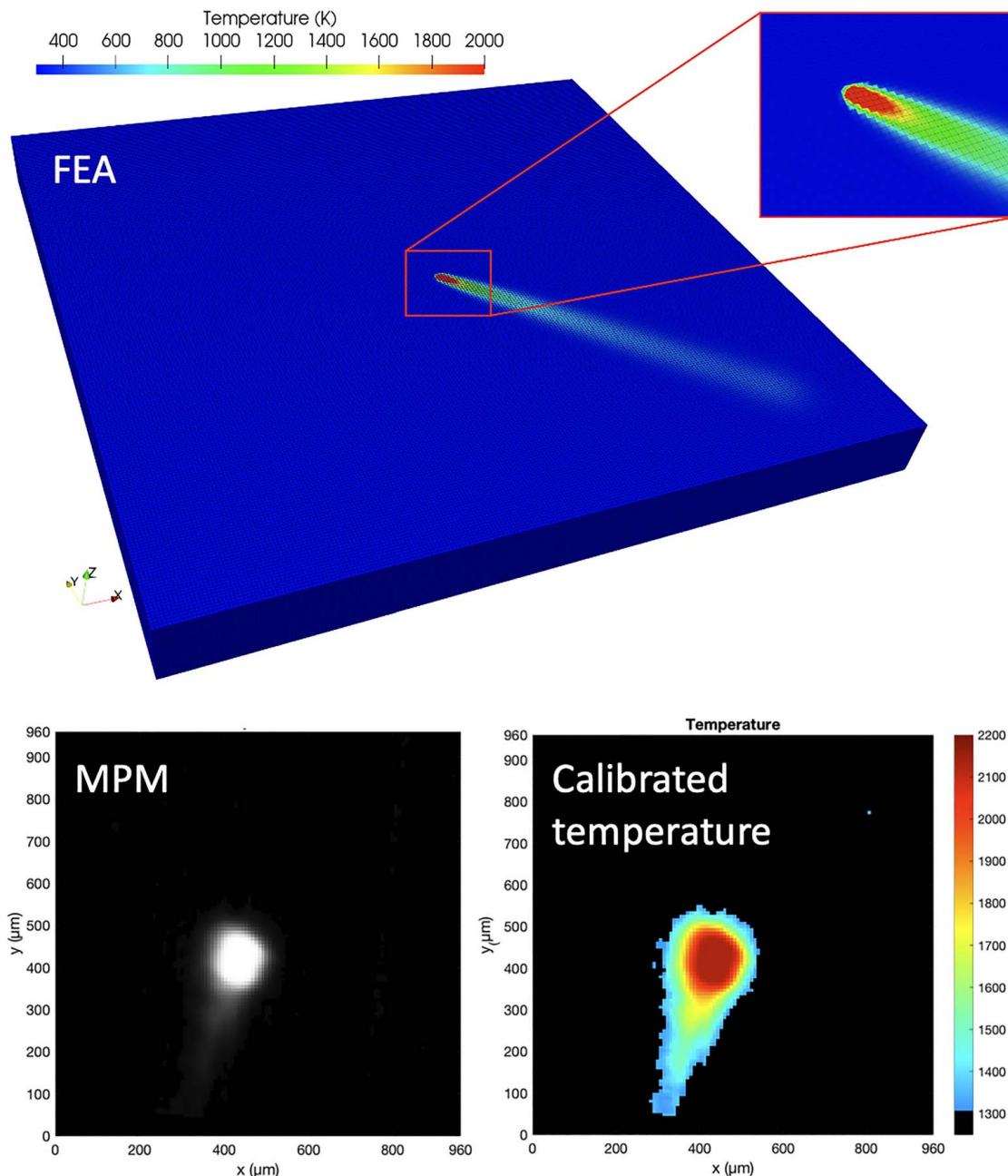


Fig. 11 Melt pool temperature profile from FEA simulation and MPM calibration

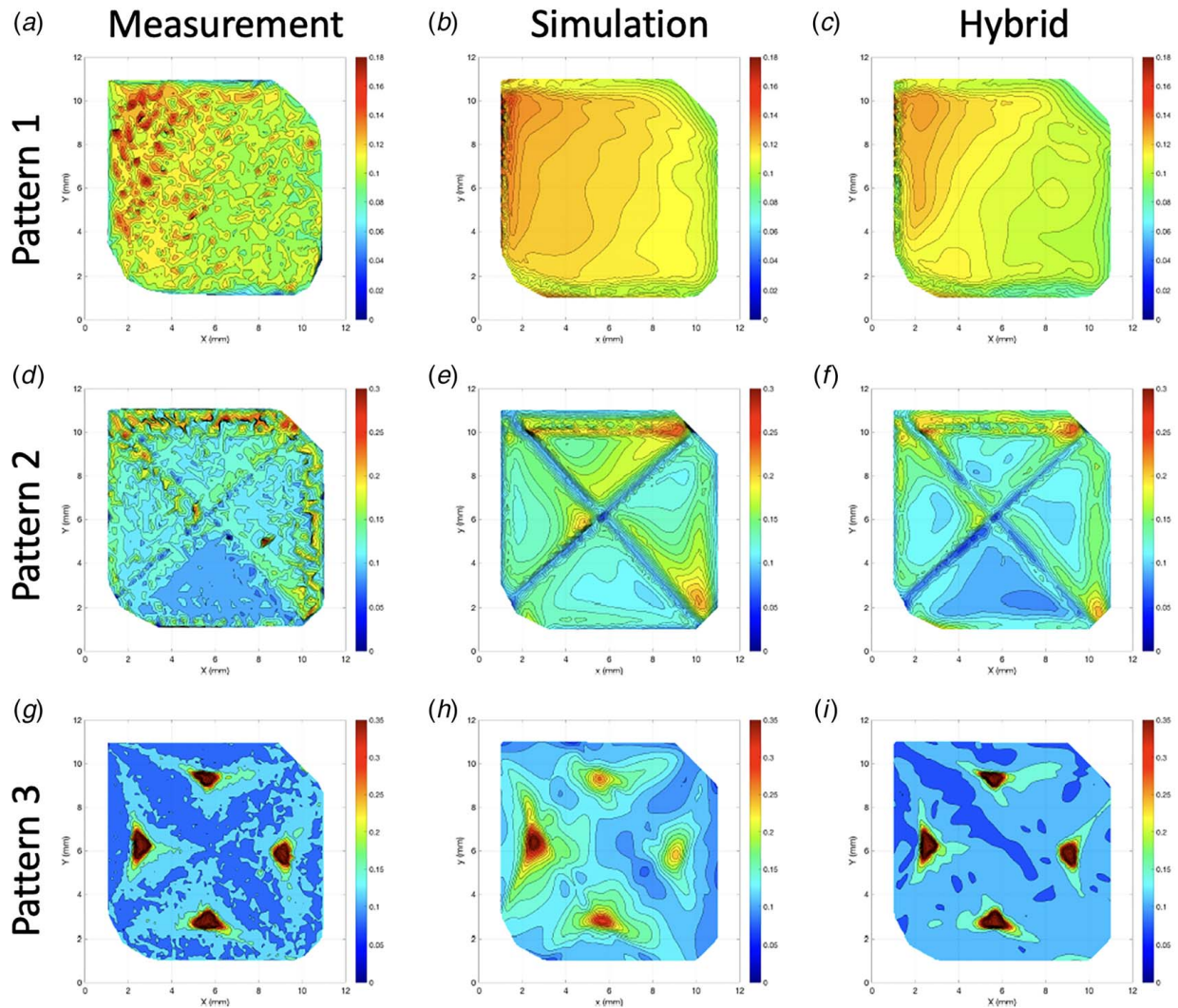


Fig. 12 Melt pool size map of the predictive: (a), (d), and (g) are measurement result of the three scan patterns, (b), (e), and (h) are results from FEA simulation, (c), (f), and (i) are the results of hybrid model

Table 2 NRMSE of simulation and hybrid models

	Pattern 1	Pattern 2	Pattern 3
Simulation	0.1170	0.1258	0.0657
Hybrid	0.0821	0.1041	0.0302
Improvement	29.83%	17.25%	54.03%

3.4 Predict Geometric Defects Caused by Overhang. This case study demonstrates a complex scenario of AM data fusion with multiple processes and datasets. The purpose is to predict the geometrical defects using both in situ and ex situ data from different builds. The biggest challenge of the typical in-process monitoring is that camera-based sensing has only 2D measurements of melt pools or build surfaces. MPM and layerwise images cannot provide information between layers or reflect changes after images are captured. A useful piece of information to predict 3D geometric defects is melt pool depth, which is missing in most in situ monitoring. To address this issue, ex situ melt pool depth measurements from earlier processes could be used to compensate for the missing part. This case study uses original MPM images to create 3D melt pool shapes by combining depth information from the earlier builds at the pointwise level. Later, the 3D melt pools obtained from the same layer are fused to layerwise 3D geometry. By fusing all the layers, the final partwise fusion provides 3D

geometric information that successfully predicts the overhang down-skin surface. The result is validated by layerwise and X-ray computed tomography (XCT) datasets.

3.4.1 Experimental Design. The experiment built four identical $5 \times 5 \times 9$ mm parts. Each part has 250 layers and a $20 \mu\text{m}$ layer thickness. Part geometry and other detailed information can be found at Lane and Yeung, 2021 and Praniewicz et al. 2020 [23,27]. There is no significant difference observed between the parts in geometry and surface roughness. One part was selected in this case study. As shown in Fig. 13, one side of the part has a cylinder hole to create the overhang conditions [13]. Overhang layers start from layer 126 to layer 226. This section focuses on predicting the geometric defect based on the penetration depth estimation of overhang layer 226. The rest will estimate the down skin of the overhang surface layer 226 to predict the geometric defects in previous layers.

3.4.2 Data Fusion Mechanism. Figure 14 details the mechanism used in this section. It combines parallel and sequential mechanisms. The process operated on the AMMT routine built the part and collected laser position and MPM images. Melt pool characterization and registration deploy the same strategies in former case studies. Similar to previous case studies, a parallel mechanism is embedded in this part for melt pool characterization.

In fact, when data were collected, either MPM or layerwise images could only describe the melt pool and part surface. No

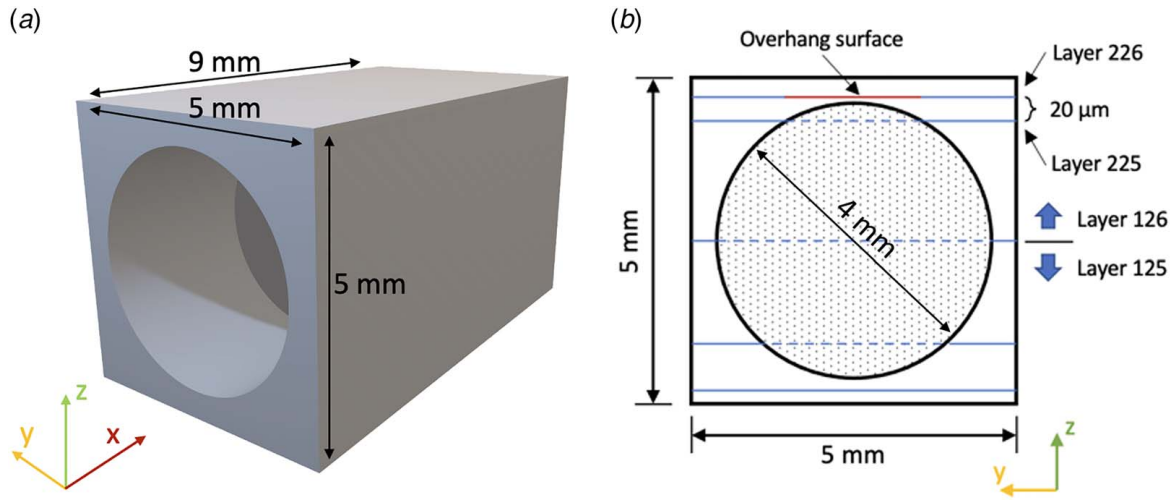


Fig. 13 Part geometry: (a) 3D view of the part showing a 3-mm cylinder hole located on side. (b) Side view of the cylinder hole. The first overhang layer is on Layer 126. Layer 226 is the last overhang layer with complete powder support.

sensor in this build can capture in situ information about the final melting status or melt pool 3D volume. 3D melt pool geometry is essential to estimate geometric defects such as overhang down-skin roughness. Thus, additional information is needed to fill this gap. Although cannot provide 3D melt pool volume, in another experiment, the EOS machine measured the melt pool width and depth under different coupons [28]. It potentially enables estimating melt pool depth from process parameters and melt pool surface characteristics. The additional process uses the same IN625

powder. Faded components in the chart indicate the missing information in both processes.

The experiment that measured the depth is on the EOS machine, which does not provide in situ measurement or scan detail as in the AMMT routine. However, an ex situ measurement of the melt pool cross-sectional area becomes available [28]. This experiment characterizes the melt pool geometric features such as statistics of width, depth, scan path, and process parameters. This information could be fused into the first system, and both experiments used the same

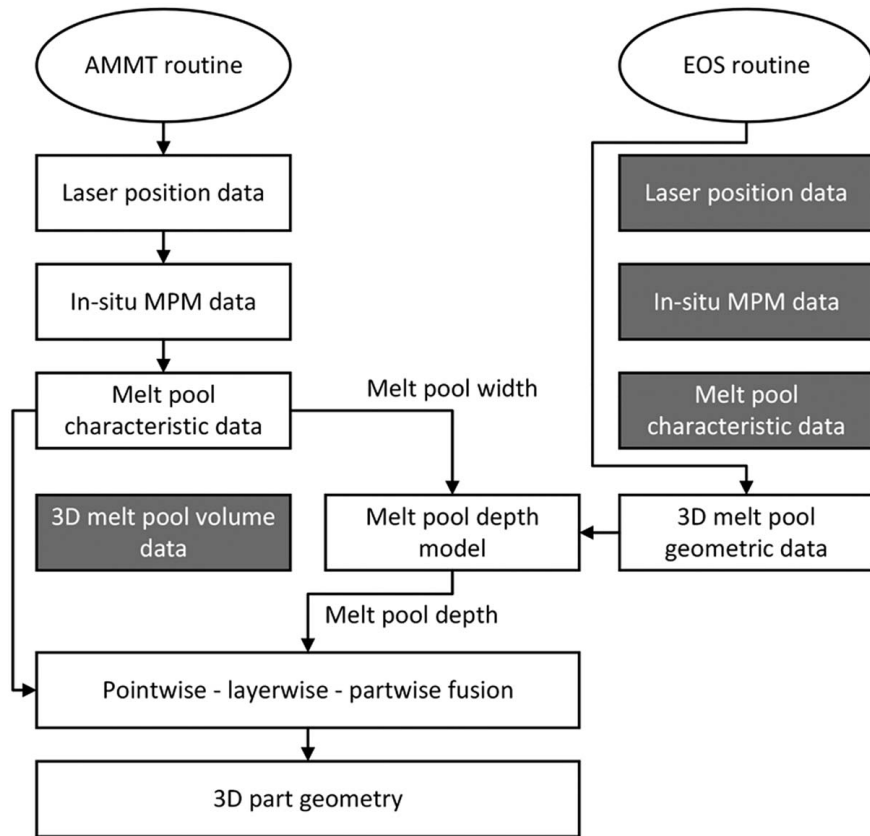


Fig. 14 Detailed mechanism to predict the 3D part geometry by experiments of two L-PBF routines. Similarly to previous two case studies. Parallel mechanism is embedded in AMMT routine to fuse melt pool features from laser position and MPM.

powder material and process parameters. Two processes provide the necessary data to establish a melt pool depth model based on process parameters and melt pool width. Partwise fusion with fully registered 3D geometric information becomes possible.

3.4.3 A Simple Approach to Estimate Melt Pool Geometry.

This subsection describes a step-by-step approach to estimating the geometric defects of the overhang down-skin surface, mainly referring to layer 226 and later layers. This case study focuses on the overhang down-skin surface. Those areas with normal part geometry would not be discussed since both the melt pool and part shape do not present noticeable defects. This subsection develops a simple physical model to roughly estimate the 3D melt pool volume, which is the critical linkage between these two processes.

Several steps are needed to estimate the geometry of layers prior to layer 226. The first step is repeating the same data fusion in Sec. 3.1 to generate the melt pool area map of layer 226. Another level of data fusion will be added to estimate the penetration depth based on a volume model. The last step incorporates penetration into previous layers to rebuild the affected geometry.

There are four steps to transform the raw MPM image to a simplified melt pool volume, as shown in Fig. 15. Thresholding is the first step to remove the background noise and small spatters. This example selected a grayscale value of 80 to find the melt pool outline. According to previous experience, the melt pool width calculated by this threshold matches the best to actual track width [10,11]. The largest connected component method separates the melt pool from larger spatters. Melt pool outline identified from edge detection would be used to approximate to simplified ellipse shape. The ellipse characterizes the melt pool width and length by the major and minor radius. The actual 3D geometry of the melt pool could be irregular and difficult to approach. Thus, this study simplified the melt pool to a half ellipsoid to reduce computational difficulties. As a result, this study uses only simplified depth-to-ellipsoid approximation. Note that melt pool depth is directly measured but would be estimated from a width–depth statistical model.

An experiment using IN625 found that the melt pool depth is $50 \pm 6 \mu\text{m}$ while the laser power is 195 W, the scan speed is 800 mm/s, the hatch distance is 0.1 mm, and the layer thickness is $20 \mu\text{m}$ [28]. These data indicate regular melt pools can penetrate two to three former layers depending on melt pool surface size and process

parameters. A linear model of melt pool depth (H) as a function of laser power (P), scan speed (V), hatch distance (D), and melt pool width (W) is shown in Eq. (1). This function is used for fast melt pool depth estimation according to the statistics in process 2. Units in this function— H is μm , P is W, V is mm/s, D is mm, and W is μm —are the same as in the original experiment [28].

$$\tilde{H} = 0.1418P - 0.0295V - 34.12D + 0.2117W + 16.17 \quad (1)$$

Equation (1) is the ideal melt pool depth model for normal process parameters and build conditions. However, this may not be directly applied to estimate melt pools located at the overhang region since they received weak support from loose powder. Evidence shows melt pools located on the overhang region tend to be much deeper [29].

From the morphological view, W , L , and H directly determine the 3D melt pool geometry. Increasing one or two coefficients will decrease the rest of the melt pool volume is similar based on the same energy input. Melt pool volume can be approximated to Eq. (2) if the melt pool shape is a simple ellipsoid. This assumption is for simplification purposes since the actual shape of the melt pool may not significantly affect the geometry if the laser continuously scans the entire part.

$$V = \frac{1}{2} \cdot \frac{4}{3} \pi \cdot \frac{1}{2} L \cdot \frac{1}{2} W \cdot H = \frac{1}{6} \pi LWH \quad (2)$$

Heat absorption and emission determine the amount of heat introduced to the powder [30]. A laser beam with the same energy density can create a larger melt pool with a higher absorption or lower emission rate. Figure 16 describes the melt pool dimensions changes under different support conditions, assuming thermal conditions are the same. Figure 16(a) shows a regular melt pool that receives normal support from the bottom. Solidified layers under the melt pool provide sufficient support from the bottom. This support resists gravity and prevents the melt pool from growing in the z -direction. Instead, the melt pool would spread larger on the xy plane. If the thermal conditions remain the same, the amount of powder being melted should be the same between Fig. 16(a) and 16(b). According to this assumption, the volume of Fig. 16(a) would be equal to Fig. 16(b). Considering the smaller W and L , H must be stretched to maintain the same volume.

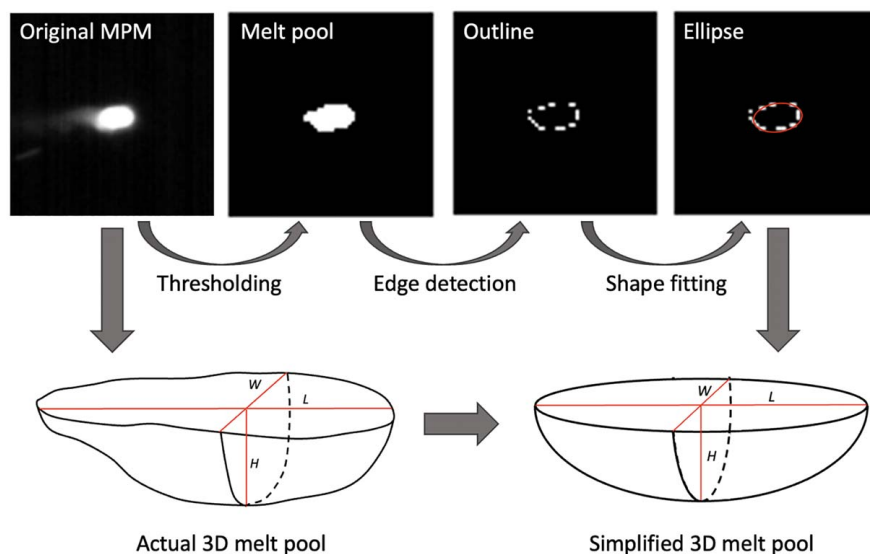


Fig. 15 Approximate the melt pool 3D geometry from original MPM image. W , L , and H are melt pool width, length, and depth. Shape fitting simplify the irregular melt pool outline to an ellipse. Simplified the melt pool geometry uses the same W , L , and H to generate the half ellipsoid.

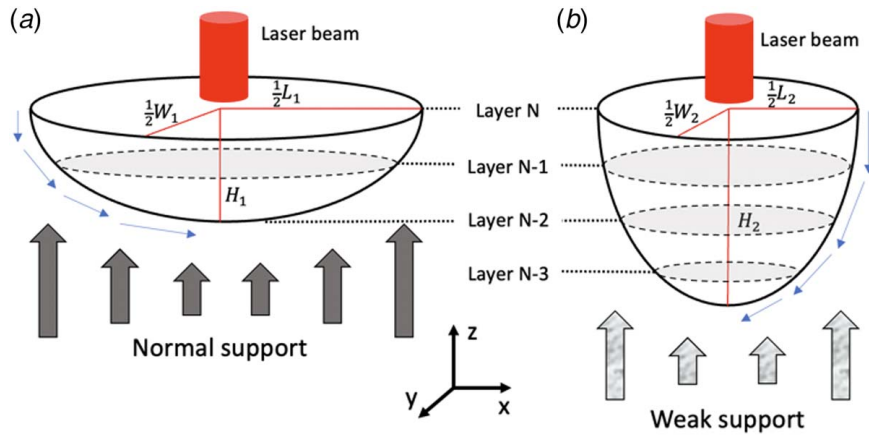


Fig. 16 Melt pool geometry comparison between wider and deeper melt pools. Gray area represents the cross-sectional area of current melt pool on previous layers.

Table 3 Measured surface dimensions of MPM images from layers 11–20

	Avg. (mm)	Std Dev. (mm)
Length (\bar{L})	0.2497	0.0470
Width (\bar{W})	0.1198	0.0169

Figure 16 also demonstrates the penetration depth of two melt pools. The melt pool in Fig. 16(a) can penetrate two layers with a larger cross-sectional area to layer N-1. However, the melt pool in Fig. 16(b) can penetrate three layers with a smaller projection on previous layers.

This case study proposes a simplified formula, Eq. (3), to calculate the melt pool depth while assuming the general amount of melting powder is the same by fixed energy input, regardless of

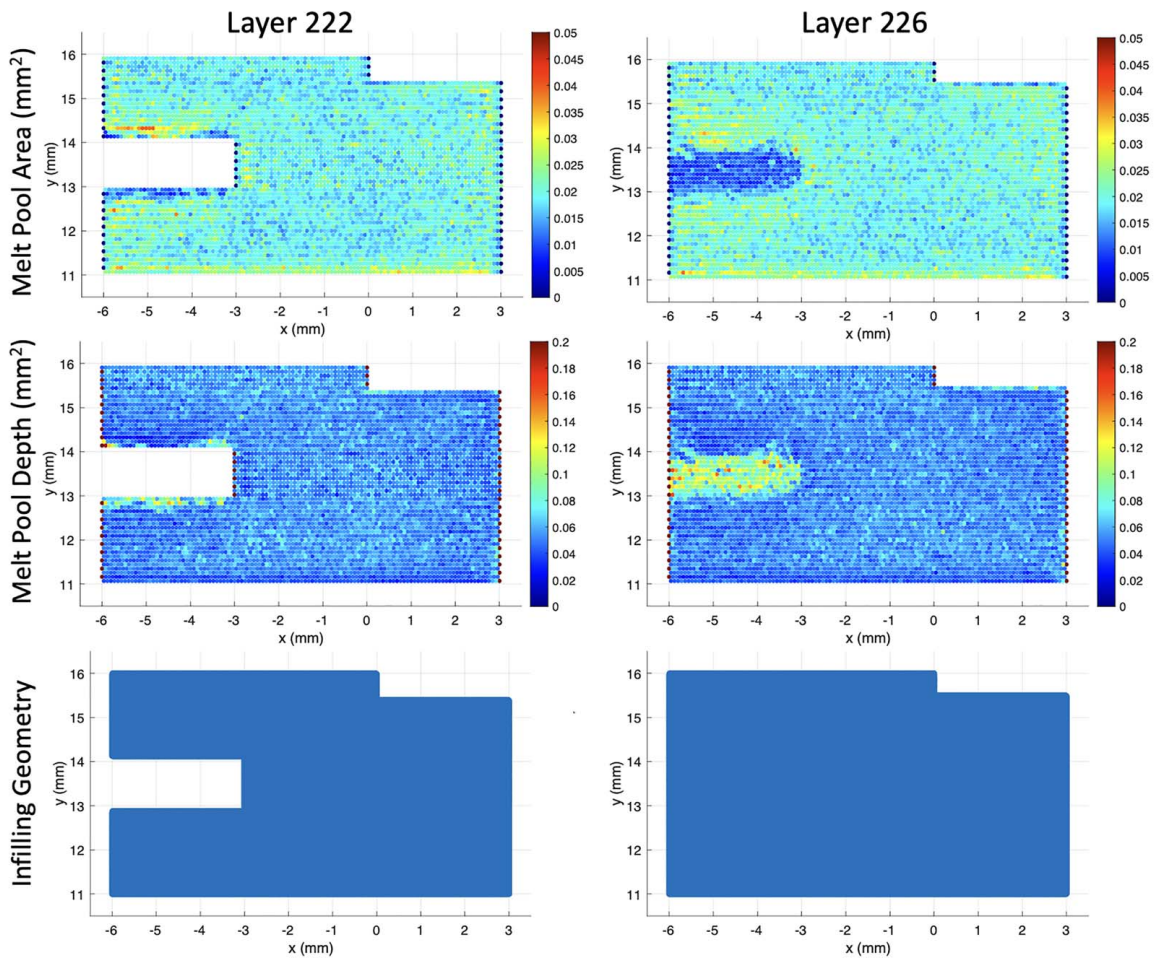


Fig. 17 Melt pool area, depth, and infilling geometry of layers 222 and 226. First row shows the melt pool measurement. Second row is the estimated depth. Third is actual area scanned.

the support level.

$$\tilde{H}_i = \frac{\frac{1}{6}\pi\bar{L}\bar{W}\bar{H}}{\frac{1}{6}\pi L_i W_i H_i} = \frac{\bar{L}\bar{W}\bar{H}}{L_i W_i H_i} \quad (3)$$

\tilde{H}_i is the predictive depth of melt pool i . \bar{L} , \bar{W} , and \bar{H} are the average length, width, and depth of normal melt pools. In this case study, the average values are calculated from 23,780 MPM images collected from layers 11–20 of the build. The reasons for choosing these images are the following:

- All selected images are captured with the same process settings.
- There is no overhang in those layers. All melt pools can be considered normal with reasonable noise.
- All layers are apart from the build plate. The initial conditions remain the same.

3.4.4 Estimated Geometric Defect—Result and Validation.

Table 3 lists the melt pool width and length of the 23,780 MPM images. The average melt pool volume is 0.00078 mm^3 , calculated from these numbers.

Figure 17 shows the melt pool area, depth, and infilling geometry of two layers. Layer 226 is the first layer on top of the cylinder hole (Fig. 13). It has a $1 \text{ mm} \times 3 \text{ mm}$ region located on the left with complete overhang conditions. The rest of this section will focus on this overhang down-skin surface. The infilling geometry plots the infilling area. The white area on the left of layer 222 is the cylinder hole. Layer 226 uses the same laser power and scan speed to infill the overhang region. The melt pool size of this region is significantly below the average. The second row of the figure shows the melt pool depth calculated from Eq. (2) and Table 3. The average melt pool depth of the overhang region is between 0.1 and 0.14 mm, indicating that the overhang melt pools on layer 226 should penetrate at least five layers. From the melt pool depth prediction, layer 222, though the laser did not melt any powder in the white area during the build, should have some solid displayed in this region.

Figure 18 analyzes the melt pool depth estimation and the interaction with previous layers. The average depth of the melt pools at the overhang region has over five layers. This is deep enough to let the melt pool of layer 226 interfere with layer 222. That is, the bottom of those melt pools would overlap previous layers, thus

changing the already formed surface. However, as mentioned in Fig. 16(b), the bottom of the melt pool has a smaller cross-section than the top surface. It means the open region in layer 222 would not be fully infilled. Layer 222 in the final part may have low-density solids in the area without laser infill.

Figure 19 provides more information about layer 222. Figure 19(a) is the laser scan path. Red that dominated the internal region, green on the top, and blue at both sides of each track represent infilling (195 w), pre-contour (100 w), and overshooting (0 W). The in situ layerwise image Fig. 19(b), captured immediately when this laser finished its scan, verifies there is no solid in the area without infill at this moment. In other words, the melting of this layer did not contribute to the geometry defect observed in XCT. It also indicates that the surface has no geometric defect at this moment. However, the ex situ XCT slice Fig. 19(c) does not agree with this conclusion. The contrast of the XCT approves the solid material dominating the area without laser scan. Disagreement between two pieces of evidence suggests layer 223 or later may be responsible for this defect. In other words, the overhang melt pool may penetrate Layer 222 to cause geometric changes. The findings have verified the prediction in Fig. 18.

This case study demonstrates the scenario with both in situ and ex situ measurement data from multiple builds. Data fusion is combined and processed to predict part quality for a build with in situ monitoring for part quality prediction. Ex situ melt pool depth measurements from an experiment on the EOS L-PBF machine are mined to a 3D melt pool model, which is applicable to the process on AMMT. The result is verified by both layerwise and XCT images. The data fusion captures the abnormal melt pools and corresponding locations, which are mainly on the overhang surface.

4 Discussion

Proposed HDFF for AM can be complex when involving multiple subprocesses and models. A successful AM data fusion requires fully aligned data integrated from different data sources, temporally and spatially. Different AM data fusion scenarios may require different data fusion mechanisms, as the paper illustrates. This framework gives guidelines on choosing the right data fusion mechanisms for various use cases. Some problems, due to data and process behavior, need to run the data fusion through multiple transformations of data to knowledge and knowledge to data.

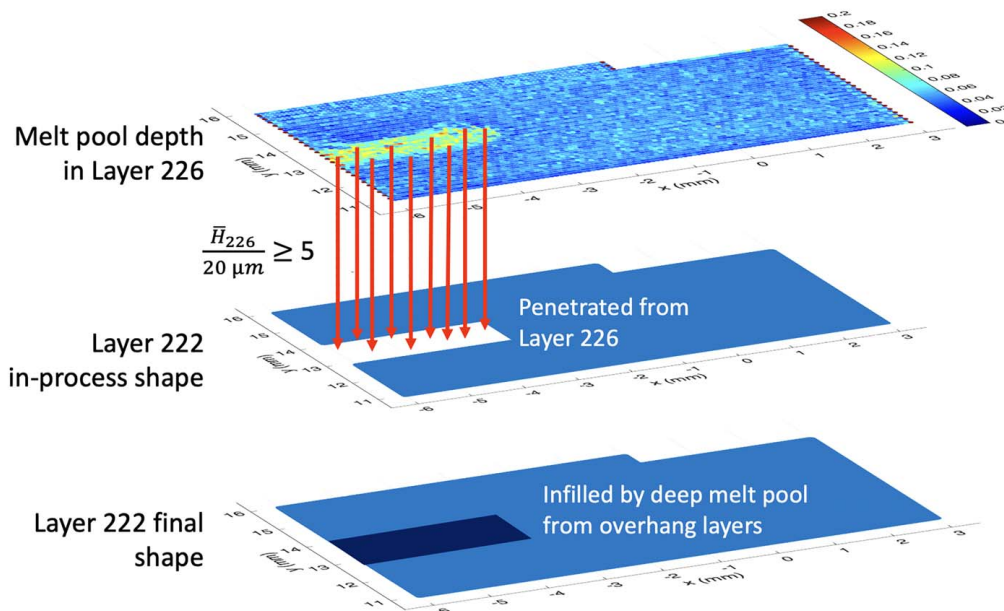


Fig. 18 Analysis of layer 222 geometry based on the melt pool depth of overhang layer 226

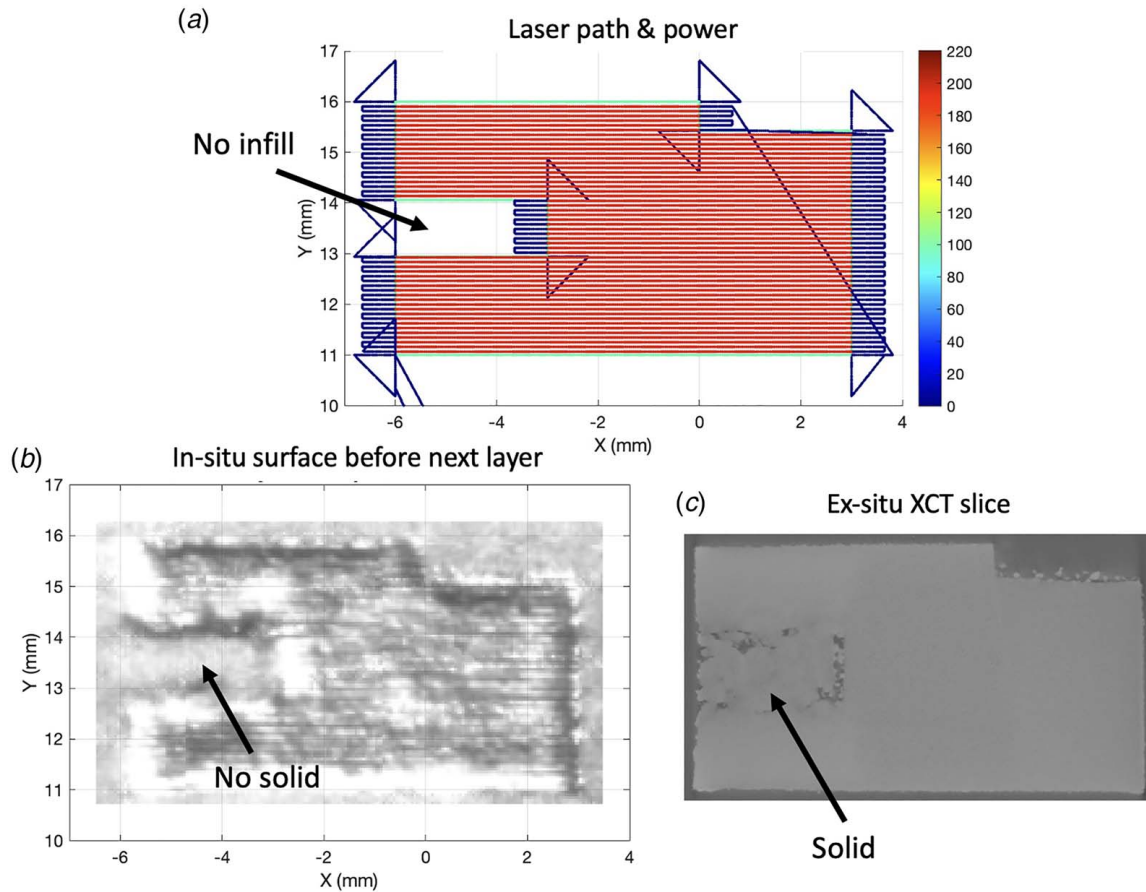


Fig. 19 Analysis of layer 222: (a) is the laser scan, (b) is in situ image captured after scanning this layer, and (c) is the ex situ XCT slice extract after the whole part has been built

AM users can use the proposed data fusion framework to solve various AM quality management problems. The scope of this method has no limitations in processes, data, and models. The main guideline is that parallel fusion mechanism is applicable when multiple datasets are captured at the same time. The spatially and temporally common characteristics between datasets are useful for extracting information out of data fusion. While the original process has missing data, users can search for related data from similar processes for quality management. Data fusion can expand the scope of the current process by leveraging knowledge and existing data.

Case studies in this paper are for demonstrative purposes. For actual AM, the case studies did not detail all the analysis. For example, the second case study builds upon two critical hypotheses. The volume may need to be more balanced with the physics. Thus, the estimated melt pool depth may need to be more accurate. Future work will focus on in situ and ex situ data fusion to reveal more useful approaches and expand the applications.

5 Conclusion

This paper presents the HDFF to aggregate multi-modal data to enhance part quality management in L-PBF. For demonstrative purposes, three case studies deploy AM data fusion to improve in-process monitoring and model predictability. The first case study verified over-melting could be identified by fusing laser position and MPM data. The second case study improved melt pool predictability by fusing simulation and experimental data. The third case study uses a more complex mechanism that involves both parallel and sequential mechanisms to fuse data from different routines and builds. The fusion between multiple processes enables the prediction of geometric defects caused by the overhanging feature.

Ex situ measurements such as microscopic, layerwise, and XCT images have verified the effectiveness. Together, these case studies highlight the flexibilities and advantages provided by the holistic data fusion framework when leveraging AM data to improve AM processes and qualify AM parts.

Acknowledgment

Certain commercial systems are identified in this paper. Such identification does not imply recommendation or endorsement by NIST; nor does it imply that the products identified are necessarily the best available for the purpose. Further, any opinions, findings, conclusions, or recommendations expressed in this material are those of the authors and do not necessarily reflect the views of NIST or any other supporting U.S. government or corporate organizations.

Funding Data

- This project is sponsored by National Institute of Standards and Technology.

Conflict of Interest

There are no conflicts of interest.

Data Availability Statement

The datasets generated and supporting the findings of this article are obtainable from the corresponding author upon reasonable request.

References

- [1] Frazier, W. E., 2014, "Metal Additive Manufacturing: A Review," *J. Mater. Eng. Perform.*, **23**(6), pp. 1917–1928.
- [2] Zhang, C., Chen, F., Huang, Z., Jia, M., Chen, G., Ye, Y., Lin, Y., et al., 2019, "Additive Manufacturing of Functionally Graded Materials: A Review," *Mater. Sci. Eng. A*, **764**, p. 138209.
- [3] McCann, R., Obeidi, M. A., Hughes, C., McCarthy, É., Egan, D. S., Vijayaraghavan, R. K., Joshi, A. M., et al., 2021, "In-Situ Sensing, Process Monitoring and Machine Control in Laser Powder Bed Fusion: A Review," *Addit. Manuf.*, **45**, p. 102058.
- [4] Williams, G., Meisel, N. A., Simpson, T. W., and McComb, C., 2022, "Analyzing Expert Design Cost Estimation for Additive Manufacturing," International Design Engineering Technical Conferences and Computers and Information in Engineering Conference, St. Louis, MO, Aug. 14–17, American Society of Mechanical Engineers, Vol. 86229, p. V03AT03A032.
- [5] Yan, W., Lu, Y., Jones, K., Yang, Z., Fox, J., Witherell, P., Wagner, G., and Liu, W. K., 2020, "Data-Driven Characterization of Thermal Models for Powder-Bed-Fusion Additive Manufacturing," *Addit. Manuf.*, **36**, pp. 101503.
- [6] Jones, K., Yang, Z., Yeung, H., Witherell, P., and Lu, Y., 2021, "Hybrid Modeling of Melt Pool Geometry in Additive Manufacturing Using Neural Networks," International Design Engineering Technical Conferences and Computers and Information in Engineering Conference, Virtual, Online, Aug. 17–19, American Society of Mechanical Engineers, Vol. 85376, p. V002T02A031.
- [7] Zhang, W., Tong, M., and Harrison, N. M., 2020, "Scanning Strategies Effect on Temperature, Residual Stress and Deformation by Multi-Laser Beam Powder Bed Fusion Manufacturing," *Addit. Manuf.*, **36**, p. 101507.
- [8] Yan, W., Ge, W., Qian, Y., Lin, S., Zhou, B., Liu, W. K., Lin, F., and Wagner, G. J., 2017, "Multi-Physics Modeling of Single/Multiple-Track Defect Mechanisms in Electron Beam Selective Melting," *Acta Mater.*, **134**, pp. 324–333.
- [9] Yeung, H., Yang, Z., and Yan, L., 2020, "A Meltpool Prediction Based Scan Strategy for Powder Bed Fusion Additive Manufacturing," *Addit. Manuf.*, **35**, p. 101383.
- [10] Yang, Z., Lu, Y., Yeung, H., and Krishnamurty, S., 2020, "From Scan Strategy to Melt Pool Prediction: A Neighboring-Effect Modeling Method," *ASME J. Comput. Inf. Sci. Eng.*, **20**(5), p. 051001.
- [11] Yang, Z., Lu, Y., Yeung, H., and Krishnamurty, S., 2020, "3D Build Melt Pool Predictive Modeling for Powder Bed Fusion Additive Manufacturing," International Design Engineering Technical Conferences and Computers and Information in Engineering Conference, Virtual, Online, Aug. 17–19, American Society of Mechanical Engineers, Vol. 83983, p. V009T09A046.
- [12] Milaat, F. A., Yang, Z., Ko, H., and Jones, A. T., 2021, "Prediction of Melt Pool Geometry Using Deep Neural Networks," International Design Engineering Technical Conferences and Computers and Information in Engineering Conference, Virtual, Online, Aug. 17–19, American Society of Mechanical Engineers, Vol. 85376, p. V002T02A037.
- [13] Yang, Z., Adnan, M., Lu, Y., Cheng, F. T., Yang, H. C., Perisic, M., and Ndiaye, Y., 2022, "Investigating Statistical Correlation Between Multi-Modality In-Situ Monitoring Data for Powder Bed Fusion Additive Manufacturing," 2022 IEEE 18th International Conference on Automation Science and Engineering (CASE), Mexico City, Mexico, Aug. 20–24, IEEE, pp. 283–290.
- [14] Hall, D. L., and Llinas, J., 1997, "An Introduction to Multisensor Data Fusion," *Proc. IEEE*, **85**(1), pp. 6–23.
- [15] Waltz, E., and Llinas, J., 1990, *Multisensor Data Fusion*, Artech house, Boston.
- [16] Ríos-Reina, R., Azcarate, S. M., Camiña, J. M., and Goicoechea, H. C., 2020, "Multi-Level Data Fusion Strategies for Modeling Three-Way Electrophoresis Capillary and Fluorescence Arrays Enhancing Geographical and Grape Variety Classification of Wines," *Anal. Chim. Acta*, **1126**, pp. 52–62.
- [17] Yang, Z., Lu, Y., Li, S., Li, J., Ndiaye, Y., Yang, H., and Krishnamurty, S., 2021, "In-Process Data Fusion for Process Monitoring and Control of Metal Additive Manufacturing," International Design Engineering Technical Conferences and Computers and Information in Engineering Conference, Virtual, Online, Aug. 17–19, American Society of Mechanical Engineers, Vol. 85376, p. V002T02A072.
- [18] Lane, B., Yeung, H., and Yang, Z., "Statistical and Spatio-Temporal Data Features in Melt Pool Monitoring of Additive Manufacturing," IISE Annual Conference, Seattle, WA, May 21–24.
- [19] Ko, H., Kim, J., Lu, Y., Shin, D., Yang, Z., and Oh, Y., 2022, "Spatial-Temporal Modeling Using Deep Learning for Real-Time Monitoring of Additive Manufacturing," International Design Engineering Technical Conferences and Computers and Information in Engineering Conference, St. Louis, MO, Aug. 14–17, American Society of Mechanical Engineers, Vol. 86212, p. V002T02A019.
- [20] Pandiyan, V., Drissi-Daoudi, R., Shevchik, S., Masinelli, G., Le-Quang, T., Logé, R., and Wasmer, K., 2022, "Deep Transfer Learning of Additive Manufacturing Mechanisms Across Materials in Metal-Based Laser Powder Bed Fusion Process," *J. Mater. Process. Technol.*, **303**, pp. 117531.
- [21] Yeung, H., Lane, B. M., Donmez, M. A., Fox, J. C., and Neira, J., 2018, "Implementation of Advanced Laser Control Strategies for Powder Bed Fusion Systems," *Procedia Manuf.*, **26**, pp. 871–879.
- [22] Lane, B., Mekhontsev, S., Grantham, S., Vlasea, M. L., Whiting, J., Yeung, H., Fox, J., et al., 2016, "Design, Developments, and Results From the NIST Additive Manufacturing Metrology Testbed (AMMT)," 2016 International Solid Freeform Fabrication Symposium, University of Texas at Austin, Austin, TX, Aug. 8–10.
- [23] Lane, B., and Yeung, H., 2020, "Process Monitoring Dataset From the Additive Manufacturing Metrology Testbed (Ammt): Overhang Part X4," *J. Res. Natl. Inst. Stand. Technol.*, **125**, pp. 1–18.
- [24] Lane, B., and Yeung, H., 2019, "Process Monitoring Dataset From the Additive Manufacturing Metrology Testbed (AMMT): Three-Dimensional Scan Strategies," *J. Res. Natl. Inst. Stand. Technol.*, **124**, pp. 1.
- [25] Yang, Z., Eddy, D., Krishnamurty, S., Grosse, I., Denno, P., Lu, Y., and Witherell, P., 2017, "Investigating Grey-Box Modeling for Predictive Analytics in Smart Manufacturing," International Design Engineering Technical Conferences and Computers and Information in Engineering Conference, Cleveland, OH, Aug. 6–9, American Society of Mechanical Engineers, Vol. 58134, p. V02BT03A024.
- [26] Moges, T., Yang, Z., Jones, K., Feng, S., Witherell, P., and Lu, Y., 2021, "Hybrid Modeling Approach for Melt-Pool Prediction in Laser Powder Bed Fusion Additive Manufacturing," *ASME J. Comput. Inf. Sci. Eng.*, **21**(5), p. 050902.
- [27] Praniewicz, M., Lane, B., Kim, F., and Saldana, C., 2020, "X-Ray Computed Tomography Data of Additive Manufacturing Metrology Testbed (AMMT) Parts: 'Overhang Part X4,'" *J. Res. Natl. Inst. Stand. Technol.*, **125**, pp. 1–9.
- [28] Ciales, L. E., Arisoy, Y. M., Lane, B., Moylan, S., Donmez, A., and Özel, T., 2017, "Laser Powder Bed Fusion of Nickel Alloy 625: Experimental Investigations of Effects of Process Parameters on Melt Pool Size and Shape With Spatter Analysis," *Int. J. Mach. Tools Manuf.*, **121**, pp. 22–36.
- [29] Charles, A., Bayat, M., and Elkaseer, A., 2022, "Elucidation of Dross Formation in Laser Powder Bed Fusion at Down-Facing Surfaces: Phenomenon-Oriented Multiphysics Simulation and Experimental Validation," *Addit. Manuf.*, **50**, p. 102551.
- [30] Lopez, F., Witherell, P., and Lane, B., 2016, "Identifying Uncertainty in Laser Powder Bed Fusion Additive Manufacturing Models," *ASME J. Mech. Des.*, **138**(11), p. 114502.